Electronic Supplementary Information (ESI)

Microstructural evolution in drying colloidal films driven by evaporation and sedimentation: Lattice Boltzmann simulation and mathematical model

Jinseong Yun, Byoungjin Chun*, Hyun Wook Jung*

Department of Chemical and Biological Engineering, Korea University, Seoul 02841, Republic of Korea

*Corresponding Authors
Prof. Hyun Wook Jung (E-mail: hwjung@grtrkr.korea.ac.kr, +82-2-3290-3306)
Dr. Byoungjin Chun (E-mail: bjchun@grtrkr.korea.ac.kr, +82-2-3290-3306)

1. Raspberry particle construction and its hydrodynamic radius

Raspberry particles were constructed by uniformly arranging surface beads on a spherical shell. The process started with an initial random distribution of N_b surface beads around a central bead, representing the core of the raspberry particle. To prevent overlap among surface beads, their interactions were governed by the Weeks–Chandler–Andersen (WCA) repulsive potential:

$$V_s(r) = \begin{cases} 4\varepsilon_s \left[\left(\dfrac{2d}{r_s} \right)^{12} - \left(\dfrac{2d}{r_s} \right)^{6} + \dfrac{1}{4} \right] & \dfrac{r_s}{2d} < 2^{\frac{1}{6}} \\ 0 & \dfrac{r_s}{2d} \geq 2^{\frac{1}{6}} \end{cases} \tag{S1}$$

where the energy scale is given by $\varepsilon_s/k_BT = 1$, the bead diameter is $d = 1\delta$, and r_s is the distance between surface beads.

To prevent rapid movements of surface beads due to overlap, the steepest descent algorithm was employed, limiting the maximum displacement of each bead to $0.01d$ per integration step. After each integration step, surface beads were repositioned onto the spherical shell along the radial direction extending from the center bead. This iterative process, repeated for 10^5 steps, ensured a uniform distribution of surface beads. Finally, the surface beads were connected to the central bead with rigid bonds, forming a single colloidal particle, at which V_s was no longer applied.

The hydrodynamic properties of the raspberry particle, specifically translational and rotational mobilities, were evaluated using the method outlined by Fisher *et al.*[1] A single raspberry particle was placed in an athermalized LB fluid within a cubic simulation box of side length L. For translational mobility measurement, a constant force F_0 was applied to the particle, while a counteracting force density of $-F_0/L^3$ was imposed on the LB fluid to ensure momentum conservation. Once the particle reached steady-state velocity v_t, the translational mobility was calculated as $\mu^T = v_t/F_0$. To extract the mobility at infinite dilution, μ^T data as a function of L were fitted to the Hasimoto form:[2] $A + B/L + C/L^3$, where A represents the translational mobility (*i.e.*, $\mu_\infty^T = 1/(6\pi\eta a_h^T)$) of an isolated particle.

Similarly, the rotational mobility $\mu^R = \omega_t/T_0$ was evaluated by applying a constant torque T_0 to a particle fixed at the center of the box and measuring its steady-state angular velocity ω_t.

To determine the mobility at infinite dilution, μ^R data as a function of L were fitted to the Hofman's expression:[3] $D + E/L^3 + F/L^{10}$, where D corresponds to the rotational mobility (*i.e.*, $\mu_\infty^R = 1/(6\pi\eta a_h^R)$) at infinite dilution. The translational and rotational hydrodynamic radii of an isolated particle were found to be $a_h^T = 1.46\delta$ and $a_h^R = 1.48\delta$, respectively, slightly smaller than the geometric radius $a = 1.5\delta$. For validation, the box size dependency of the dimensionless translational and rotational mobilities were compared with numerical results from Hofman *et al.*,[3] as shown in Fig. S1. To reduce computational costs, hollow raspberry particles filled with fluid were used. Although Fischer *et al.*[1] showed that filled raspberry particles with internal beads offered more accurate hydrodynamic interactions, the difference was minimal, justifying the use of hollow raspberry particles.

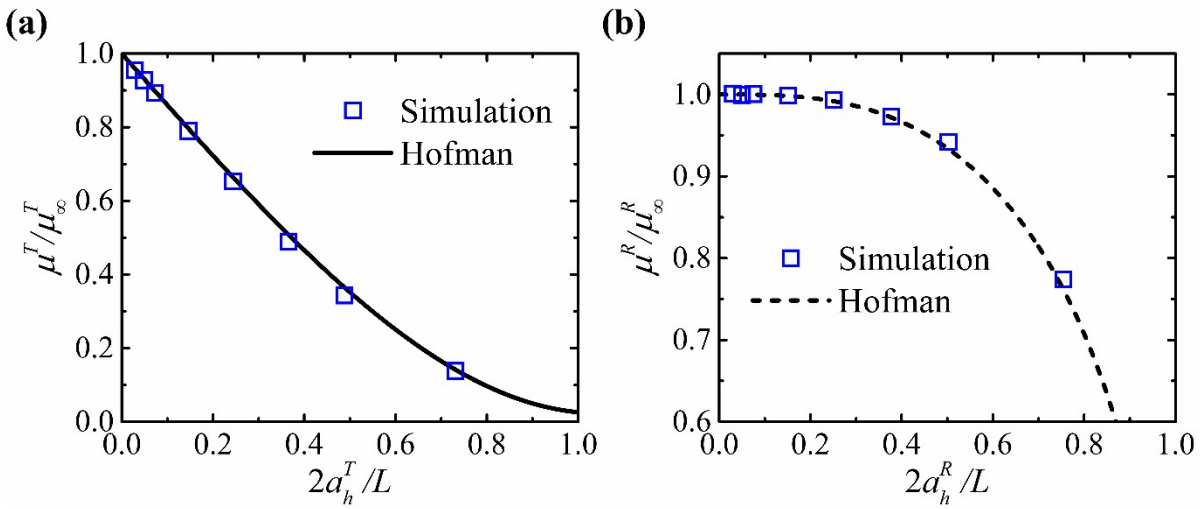

Fig. S1 Dependency of the simulation box side length L on the dimensionless (a) translational and (b) rotational mobilities of the raspberry particle. The solid curve in (a) represents the fitting curve derived from the numerical data of Hofman *et al.*,[3] while the dashed curve in (b) corresponds to the analytical expression provided by Hofman *et al.*[3]

2. Effects of particle concentration on interparticle interaction

The choice of the repulsive potential to prevent particle overlap was arbitrary. To mitigate potential artifacts in the structural analysis of the particle system, a hard-sphere repulsive force (HSF), designed similarly to polystyrene latex sphere,[4] was introduced as a particle-pair interaction (eqn (10)) instead of the widely used WCA potential.[5] Here, additional simulations were performed equilibrating HSF-applied particles at different bulk concentrations, ϕ_{bulk}, within a periodic cubic box with side length of $L = 20a$. The structure of the particles was analyzed in variation of ϕ_{bulk}, and the results were compared with those obtained using WCA potential (eqn (S2)) as follows:

$$V_{WCA}(r) = \begin{cases} 4\varepsilon\left[\left(\frac{2a}{r}\right)^{12} - \left(\frac{2a}{r}\right)^{6} + \frac{1}{4}\right] & \frac{r}{2a} < 2^{\frac{1}{6}} \\ 0 & \frac{r}{2a} \geq 2^{\frac{1}{6}} \end{cases}, \tag{S2}$$

where energy scale of the potential is set to $\varepsilon = 10k_BT$.

Figure S2a shows the radial distribution function, $g(r)$, of particles for $\phi_{bulk} = 0.3$ and $\phi_{bulk} = 0.5$, where the results using the HSF (blue curve) are contrasted with those using the WCA potential (red dot-dashed curve). The location of the first peak of $g(r)$ indicates the effective particle size. The larger effective particle size observed with the WCA potential was attributed to the longer range of repulsive interactions compared to the HSF. Notably, for the HSF, the first peak of $g(r)$ was consistently located at $r/2a = 1.03$ for both $\phi_{bulk} = 0.3$ and $\phi_{bulk} = 0.5$. In contrast, for the WCA potential, the position of the first peak of $g(r)$ decreased from $r/2a = 1.13$ to 1.10 as ϕ_{bulk} increased from 0.3 to 0.5. The reduction in the effective particle size with increasing ϕ_{bulk} for the WCA potential suggests that particle deformation occurred at higher concentrations. The relative insensitivity of the HSF model to concentration variations makes it more suitable for processes involving significant concentration changes, such as drying.

The simulation results comparing vertical particle distributions during drying, utilizing HSF (blue curve) against the WCA potential (red dot-dashed curve), under the conditions of $\phi_0 = 0.1$ and $Pe = Pe_{sed} = 100$, are presented in Fig. S2b. Initially, the discrepancy between results was negligible. However, at later times, notable differences in the local particle concentrations emerged, particularly at the top and bottom of the film, where particle accumulation was pronounced. Specifically, at $\bar{t} = 0.6$, the HSF results demonstrated higher local concentrations

at both the top and bottom of the film. This was attributed to the smaller effective particle size in HSF, which facilitated denser packing compared with the WCA potential. At the end of the wet stage ($\bar{t}_f = 0.84$), the higher ϕ at the top of the film for the HSF relative to the WCA potential led to a lower ϕ at the bottom due to concentration conservation.

In situations where the dilute regime is maintained, the choice of interparticle interaction has little impact on the particle distribution. However, as the particle concentration increases, the final film microstructure is significantly affected. Consequently, an interparticle interaction that closely resembles hard-sphere particles, such as HSF, is deemed suitable for simulations involving drying and sedimentation because it is less affected by concentration changes.

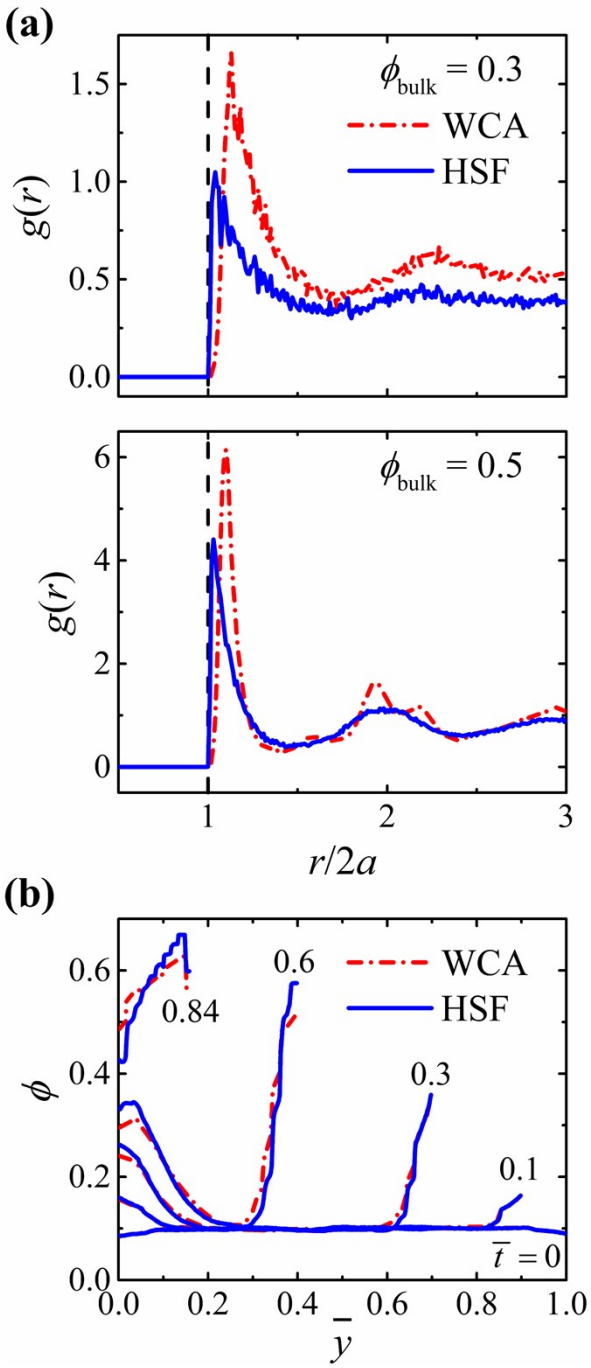

Fig. S2 Comparison of simulation results using HSF (blue curves) and WCA potential (red dot-dashed curves). (a) The radial distribution functions $g(r)$, for particles equilibrated within a periodic box, are shown at $\phi_{bulk} = 0.3$ and 0.5, respectively. (b) The time evolutions of particle distributions during drying using HSF were compared to those using WCA potential under conditions of $\phi_0 = 0.1$, $Pe = 100$, and $Pe_{sed}/Pe = 1$.

3. Comparison of LB simulation results and model predictions on the time evolution of particle distribution

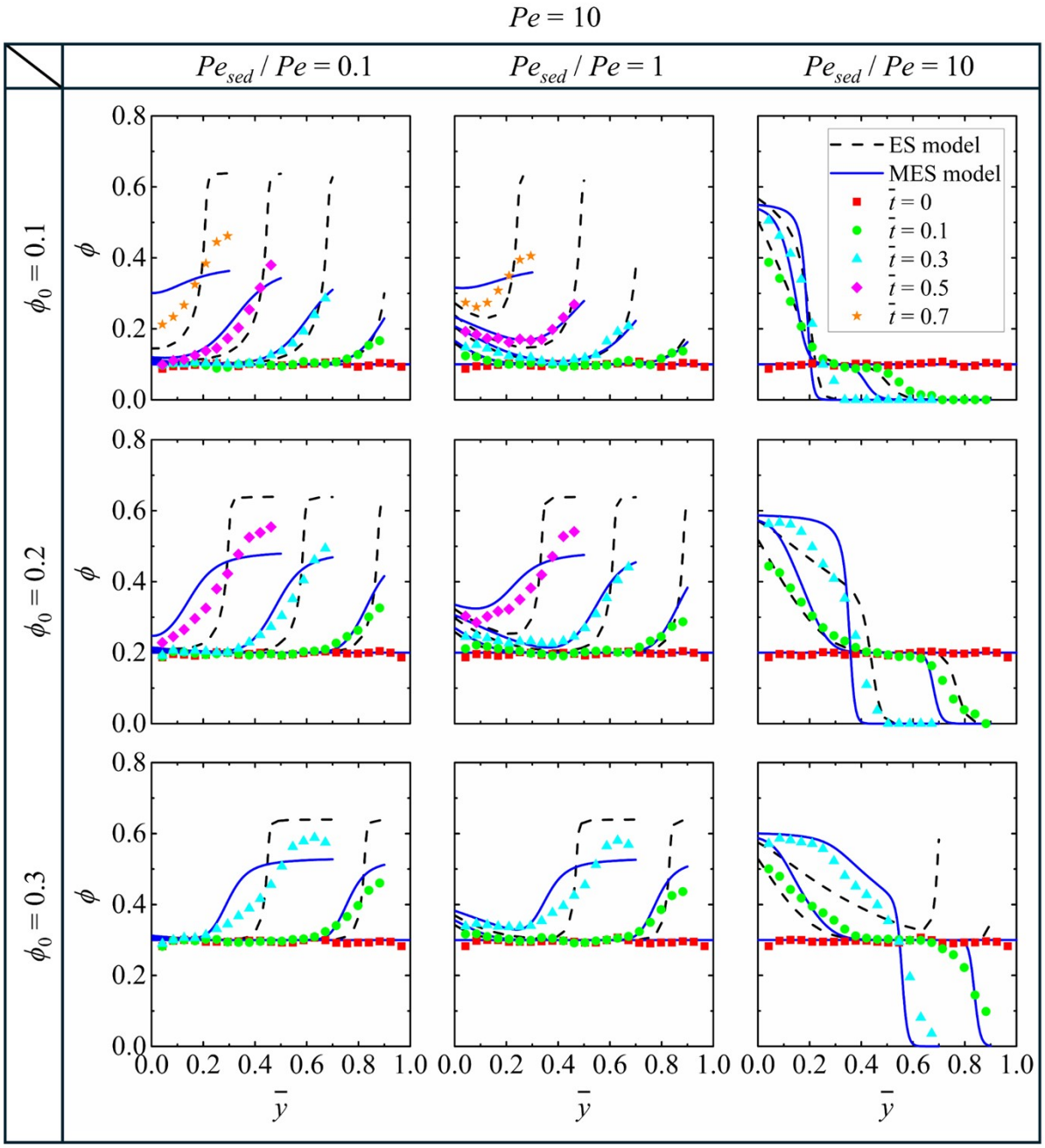

Fig. S3 Time evolutions of particle volume fraction profiles of LB simulation are compared with the predictions of MES and ES models with variations in ϕ_0 from 0.1 to 0.3 and Pe_{sed}/Pe from 0.1 to 10 at Pe = 10. The symbols represent the results of LB simulation at different dimensionless times ($\bar{t}$ = 0–0.7). The results of MES and ES models at each time are presented in blue solid curves and black dashed curves, respectively.

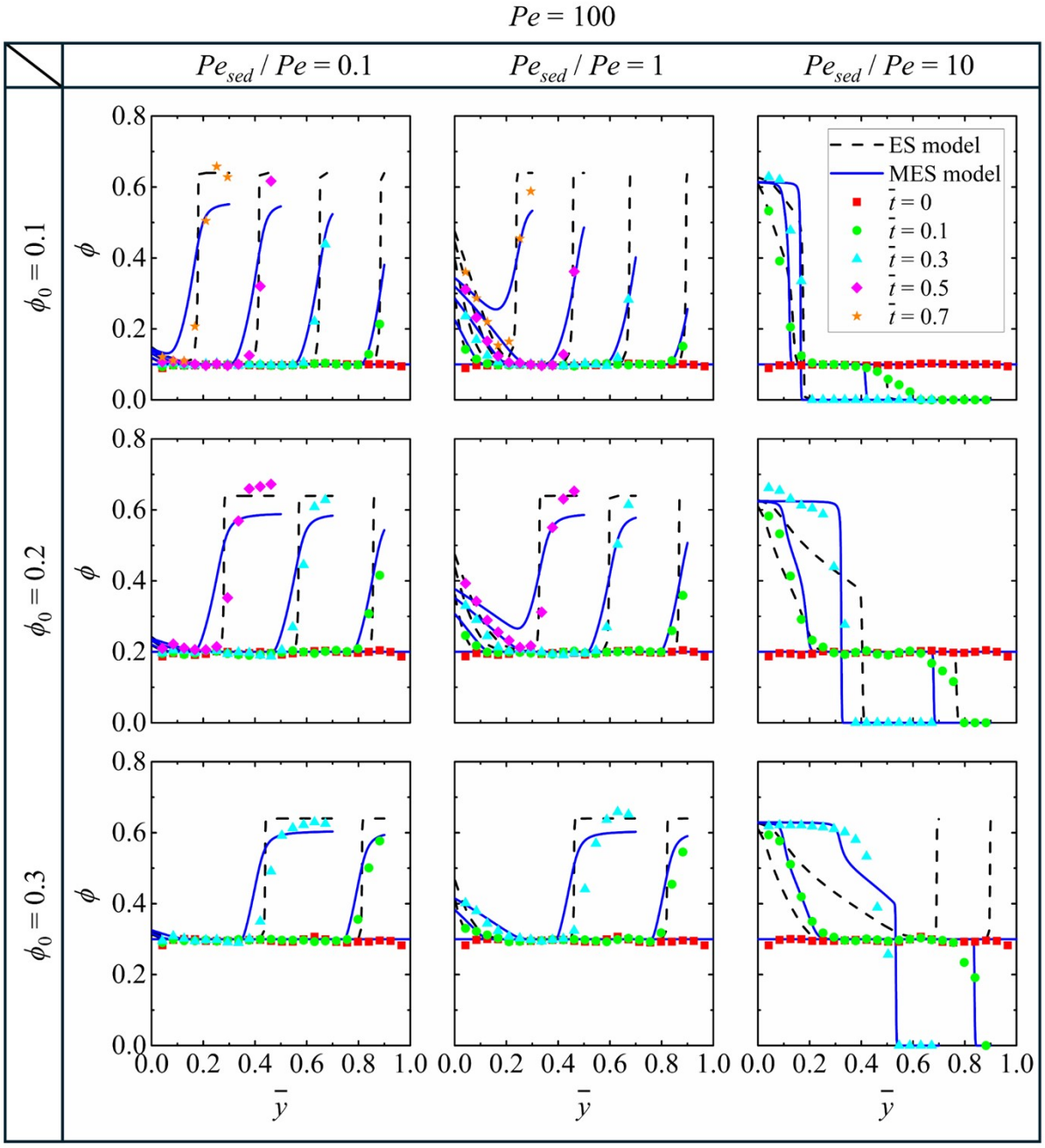

Fig. S4 Time evolutions of particle volume fraction profiles from LB simulations are compared with predictions of MES (blue solid curves) and ES models (black dashed curves), with variation of ϕ_0 = 0.1–0.3 and Pe_{sed}/Pe = 0.1–10 at Pe = 100. The symbols represent the results of LB simulation at different $\bar{t}$ ranging from 0 to 0.7.

References

1. L. P. Fischer, T. Peter, C. Holm and J. de Graaf, *J. Chem. Phys.*, 2015, **143**, 084107.

2. H. Hasimoto, *J. Fluid Mech.*, 1959, **5**, 317–328.

3. J.M.A. Hofman, H.J.H. Clercx, P.P.J.M. Schram, *Physica A*, 1999, **268**, 353–390.

4. G. Bossis and J. F. Brady, *J. Chem. Phys.*, 1984, **80**, 5141–5154.

5. H.C. Andersen, J.D. Weeks, D. Chandler, *Phys. Rev. A*, 1971, **4**, 1597–1607.